Ab initio complex band structure of conjugated polymers: Effects of hydrid density functional theory and *GW* schemes

Andrea Ferretti,[1,*] Giuseppe Mallia,[2] Layla Martin-Samos,[3] Giovanni Bussi,[3,4] Alice Ruini,[1,5]
Barbara Montanari,[6] and Nicholas M. Harrison[2,7]
[1]*Centro S3, CNR–Istituto Nanoscienze, I-41125 Modena, Italy*
[2]*Department of Chemistry, Imperial College London, London SW7 2AZ, UK*
[3]*CNR–IOM Democritos, I-34014 Trieste, Italy*
[4]*Scuola Internazionale Superiore di Studi Avanzati, SISSA via Bonomea 265, I-34136 Trieste, Italy*
[5]*Dipartimento di Fisica, Università di Modena e Reggio Emilia, I-41125 Modena, Italy*
[6]*Computational Science and Engineering Department, STFC Rutherford Appleton Laboratory, Oxfordshire OX11 0QX, UK*
[7]*Computational Science and Engineering Department, STFC Daresbury Laboratory, Cheshire WA4 4AD, UK*
(Received 8 February 2012; published 4 June 2012)

The nonresonant tunneling regime for charge transfer across nanojunctions is critically dependent on the so-called β parameter, governing the exponential decay of the current as the length of the junction increases. For periodic materials, this parameter can be theoretically evaluated by computing the complex band structure (CBS)—or evanescent states—of the material forming the tunneling junction. In this work we present the calculation of the CBS for organic polymers using a variety of computational schemes, including standard local, semilocal, and hybrid-exchange density functionals, and many-body perturbation theory within the *GW* approximation. We compare the description of localization and β parameters among the adopted methods and with experimental data. We show that local and semilocal density functionals systematically underestimate the β parameter, while hybrid-exchange schemes partially correct for this discrepancy, resulting in a much better agreement with *GW* calculations and experiments. Self-consistency effects and self-energy representation issues of the *GW* corrections are discussed together with the use of Wannier functions to interpolate the electronic band structure.

DOI: 10.1103/PhysRevB.85.235105 PACS number(s): 72.10.−d, 71.20.Rv

I. INTRODUCTION

The fields of molecular electronics and charge transport through nanojunctions have been extensively investigated in the past 15 years.[1–3] At the experimental level many techniques have been developed, including those based on break junctions, nanostructured and scanning probe layouts, and self-assembled monolayers.[3,4] Significant improvements in the accuracy with which these junctions are characterized have been achieved over the years, e.g., to address the *I-V* characteristics of single molecular junctions. Moreover, a large experimental literature exists[5–7] on nonresonant tunneling experiments, where it is possible to determine the exponential decay (β_0) of the current $I = I_0 \exp(-\beta_0 L)$ as a function of the length L of the tunneling layer, e.g., a layer of organic self-assembled monolayers connected to metallic electrodes. Even though the β_0 parameter also depends[6,8–10] on the detailed nature of the interface, it carries mostly information about the properties of the tunneling layer itself, which makes β_0 an interesting analysis and characterization tool.

Experimentally, these measurements are performed using different setups, ranging from metal-insulator-metal (MIM) junctions, as mentioned above, to the evaluation of kinetic constants of electrotransfer reactions (optically or electrochemically induced) in donor-bridge-acceptor molecular complexes.[11–15] In terms of systems, measurements have been performed on a number of cases, ranging from saturated olephins (alkanes)[5,12,13] to biological molecules (such as DNA).[16–18] Theoretically, the electronic mechanism underlying these experiments has been analyzed and understood.[1,5,8,10] As stated in Ref. 8, the key parameter β can be expressed (e.g., in MIM junctions) in terms of (i) the band gap E_g and the (frontier) band widths (or hopping parameter) t of the insulating layer and (ii) the alignment of the Fermi level in metals with the energy gap of the insulator. Indeed, the effect of the electronic structure of the insulating layer can be singled out by evaluating[8] the complex band structure (CBS), or evanescent states, in the limit of an infinitely long insulating region. The CBS approach is also particularly interesting for an *ab initio* evaluation of β, where the calculations can be performed using either wave-function-based[19] or Green's-function-based[8] approaches. A scheme describing the relation between the electronic structure of the MIM junction and the evaluation of the β-decay factor is shown in Fig. 1.

Nevertheless, since the β parameter can be[8] directly related to the ratio between the energy gap and the band width of the insulator layer, the accuracy of standard electronic-structure simulations based on the Kohn-Sham (KS) framework of the density functional theory (DFT) can be questioned. In fact, using eigenvalues computed from the KS-DFT it is well known that the fundamental band gap is badly underestimated and (when using local and semilocal approximations) the delocalization of electronic states is typically overestimated. Moreover, the description of this class of experiments in terms of single-particle energies would require them to be interpreted as quasiparticle (QP) energies, in order to address the electronic dynamics of the system. This is valid for advanced MBPT methods,[20] such as Hedin's *GW* approximation,[21,22] and, at least in a perturbative sense, also for Hartree-Fock (HF) calculations. However, KS-DFT states are fictitious orbitals with no direct physical interpretation, and their use in this context can only be justified by the assumption that the

 ©2012 American Physical Society

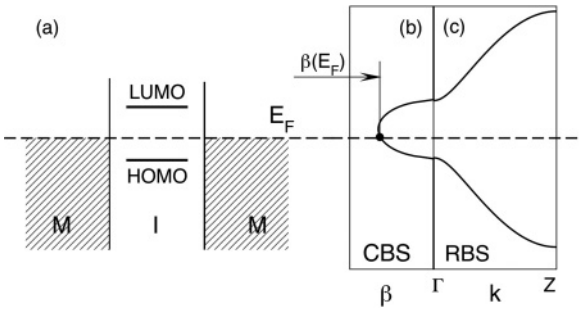

FIG. 1. Nonresonant tunneling experiment. (a) Scheme of the alignment of electronic levels in a metal-insulator-metal (MIM) junction. (b) Complex band structure (CBS) and (c) real band structure (RBS) corresponding to the (extended) insulator system. The computed value to be compared with experiments is highlighted as $\beta(E_F)$, E_F being the Fermi energy of the MIM junction.

exchange-correlation kernel is an approximation for the QP Hamiltonian. Model self-energies have also been used recently[23] to correct the electronic structure of metal-molecule-metal junctions and found to be important for the evaluation of β. To date there has been no systematic investigation of the performance of different *ab initio* schemes in the calculation of β-decay factors.

In this paper we study the effects of hybrid exchange-correlation functionals[24] and the *GW*[21,22] approximation on the calculation of β-decay factors, according to a scheme based on the CBS formalism.[8] A detailed comparison with local and semilocal functionals is also provided. The theoretical background of CBS and *GW* and hybrid functionals is described in Secs. II and III, respectively. We discuss a general application of the Wannier function (WF) interpolation to the case of a *GW* electronic structure (Sec. III B). Our approach is applied to a number of polymers as reported in Fig. 2: We compute

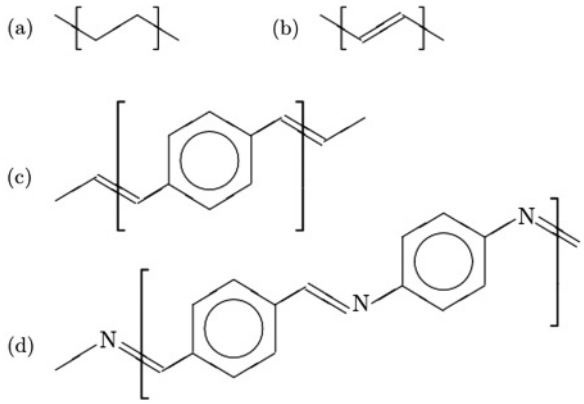

FIG. 2. Polymers studied: (a) PE (polyethylene), with each carbon atom in the polymer chain being fully saturated by two hydrogen atoms; (b) PA (polyacetylene), where sp^2 hybridization of carbon atoms in the chain (each one also bonded to one hydrogen atom) implies π conjugation, i.e., alternation of single and double C–C bonds along the chain; (c) PPV [poly-(*para*-phenylene-vinylene)], constituted by benzene rings connected through vinyl groups, also presenting conjugation; (d) PPI [poly-(phenylene-imine)], differing from PPV in the substitution of one carbon atom in each vinyl group by a N atom, which still preserves the polymer conjugation.

the CBS for polyethylene (PE) and polyacetylene (PA) as references for saturated and conjugated chains, respectively. We then consider poly-(*para*-phenylene-vinylene) (PPV)[25] and poly-(phenylene-imine)[7,26] (PPI), which are relevant from a technological point of view, and we also make a comparison with recent experimental data.[7] All chains are studied as isolated; see Appendix B for full numerical details.

II. METHOD: TRANSPORT

To simulate the decay factors of nonresonant tunneling experiments we adopt the CBS algorithm proposed by Tomfohr and Sankey.[8] For a recent discussion of the connection of transport properties with the CBS theory, see also the work by Prodan and Car.[10] Within this approach, we need to evaluate the CBS in the limit of an infinitely thick insulating region (β is in fact an asymptotic behavior). The outcome of this procedure is a set of $\beta(E)$ curves. The value β_0 which has to be compared with the experiments is the smallest one (i.e., the most penetrating) aligned with the Fermi level of the junction:

$$\beta_0 = \beta(E_F). \tag{1}$$

Since the electrodes are not considered in the calculation, together with the proper metal-insulator interface, E_F is not known *a priori* and must be either estimated or calculated separately. This issue is discussed in detail in Ref. 8. In the present work we do not compute the Fermi level alignment explicitly, and we rely on the estimation method proposed in the above reference,[8] which consists in evaluating $\beta(E)$ at the energy where $d\beta/dE = 0$ (branch point). This method is originally due to Tersoff[27] and based on the pinning of E_F by metal-induced gap states (MIGSs). We discuss this approximation in Sec. V, where we compare it with experimental results. Note that the value of β at the branch point is also connected (for nonmetallic one-dimensional systems with a local potential) with the degree of localization of the density matrix, since β determines[28,29] its spatial decay. Pictorially, a better description of $\beta(E)$ means, then, an improved description of the electronic localization.

Scanning the energy spectrum, the CBS procedure searches for evanescent solutions to a given effective single-particle Hamiltonian. By definition, states with (real) Bloch symmetry $\mathbf{k}$ satisfy the relation

$$\hat{T}(\mathbf{R})\,\psi_{\mathbf{k}}(\mathbf{r}) = \psi_{\mathbf{k}}(\mathbf{r}+\mathbf{R}) = \lambda\,\psi_{\mathbf{k}}(\mathbf{r}), \tag{2}$$

where $\mathbf{R}$ is any direct lattice vector, $\hat{T}(\mathbf{R})$ is a translation operator, and $\lambda = e^{i\mathbf{k}\cdot\mathbf{R}}$. In the same way it is possible to define a *complex* Bloch symmetry $\boldsymbol{\kappa} = \mathbf{k} + i\boldsymbol{\beta}/2$ setting $\lambda = e^{i\boldsymbol{\kappa}\cdot\mathbf{R}} = e^{i\mathbf{k}\cdot\mathbf{R}}\,e^{-\boldsymbol{\beta}\cdot\mathbf{R}/2}$, which is thus no longer a pure phase. The imaginary part of $\boldsymbol{\kappa}$ implies a real-space exponential decay of the wave functions and it is customary to define $\beta(E) = 2\,|\mathrm{Im}[\boldsymbol{\kappa}(E)\cdot\hat{e}]|$ ($\hat{e}$ is the transport direction). The energy dependence of κ comes from the fact that, for a fixed energy E, the solutions are searched in terms of $\boldsymbol{\kappa}$, as is usually done in scattering theory.

By adopting a localized basis set $\{|\phi_{i\mathbf{R}}\rangle\}$ (i and $\mathbf{R}$ are orbital and lattice indexes, respectively), it is possible to define the Hamiltonian H and overlap S operators through their matrix elements $H_{ij}(\mathbf{R}) = \langle\phi_{i\mathbf{0}}|H|\phi_{j\mathbf{R}}\rangle$ and $S_{ij}(\mathbf{R}) = \langle\phi_{i\mathbf{0}}|\phi_{j\mathbf{R}}\rangle$, and the wave functions as $|\psi_l\rangle = \sum_{i\mathbf{R}} C_{il}(\mathbf{R})\,|\phi_{i\mathbf{R}}\rangle$. Setting

$Z = H - ES$, the eigenvalue equation for H can be written as

$$\sum_{m=-N}^{N} Z(\mathbf{R}_m)C(\mathbf{R}_m) = 0, \tag{3}$$

where matrix multiplication is implicit, and N is the number defining the last nonzero matrix $Z(\mathbf{R}_N)$. Here we are assuming a real-space decay of the Hamiltonian and overlap matrices, which is typically physical, even if the range can be strongly dependent on the scheme used to define the Hamiltonian. We comment on this point later when discussing the use of *GW* or HF methods. It is then possible to derive[8] the system of $2N$ matrix equations

$$-\sum_{m=-N}^{N-1} Z(\mathbf{R}_m)C(\mathbf{R}_m) = Z(\mathbf{R}_N)\,\lambda C(\mathbf{R}_{N-1}), \tag{4}$$

$$C(\mathbf{R}_{m+1}) = \lambda C(\mathbf{R}_m), \quad m = -N, N-2, \tag{5}$$

where Eq. (5) is a direct consequence of Eq. (2). Such matrix equations become an eigenvalue problem for λ, assuming we can invert the matrix $Z(\mathbf{R}_N)$. As pointed out in Ref. 8, this is very often not the case, as the matrix is singular, but the singluarities can be avoided. The reader is referred to the original work for the details. The full algorithm proposed in Ref. 8 has been implemented in the WANT code[30,31] and used in the present work. A simple tight-binding analytical model (a generalized version of the one presented in Ref. 8) is discussed in Appendix A. This model is used in Sec. IV to fit and interpret the real and CBSs of the polymers we have investigated here.

III. METHOD: ELECTRONIC STRUCTURE

According to the above discussion, in order to simulate the decay coefficient of an MIM junction, we need to compute the electronic structure of the insulating layer (considered to be infinitely extended). The underlying reason for this simplification is that we interpret the computed single-particle energies of the system as QP energies, which, in turn, determine the dynamics of singly charged excitations. In general, the transport problem for interacting systems is more complicated than that and requires a more sophisticated treatment.[32–40] For DFT, the understanding of how the exact KS-DFT Hamiltonian performs to compute transport has recently been the subject of several investigations.[41–44] Apart from the properties of the exact functional, currently available DFT approximations like the LDA and GGA have been demonstrated to systematically overestimate the conductance, especially for off-resonant junctions.[32,45,46] Pragmatically, this suggests that corrections beyond local and semilocal KS-DFT approaches are needed.

Using QP-corrected electronic structure to compute charge transport (e.g., by means of the Landauer formula)[47] through interacting systems seems to be a reasonable approximation when finite-lifetime effects are weak.[37,48] Indeed, a number of works computing QP energies by means of the *GW* approximation[35,49–52] or model self-energies[23,53–55] have been reported in the literature. On the other hand, hybrid-exchange functional methods like B3LYP[56] and PBE0[57] are widely used and lead to band gaps and band widths which are usually closer[58] to the experimental values than simple semi-local KS approaches, for both molecules and solids. Recent works[59–62] have further investigated the accuracy of hybrid exchange functionals, also in comparison with *GW* calculations. In this work we compare *GW* and hybrid functionals for the calculation of electronic structure and transport properties of selected organic polymers. In the following we summarize the *GW* approximation and underline some formal similarities with hybrid functionals.

A. The *GW* approximation and hybrid DFT

A many-body theoretical formulation of the electronic structure problem can be obtained using the Green's function formalism. The one-particle excitation energies of an interacting system are the poles of its interacting Green's function $G(E)$,[20,63] which can be written as

$$G(E) = [EI - h_0 - \Sigma(E)]^{-1}, \tag{6}$$

where h_0 is an effective single-particle Hamiltonian and $\Sigma(E)$ is the nonlocal, non-Hermitian, frequency-dependent self-energy operator. In general, Σ is not known *a priori* and must be approximated. In this work the self-energy is computed within the *GW* approximation:[21,22]

$$\Sigma_{\mathrm{GW}}(\mathbf{r}_1,\mathbf{r}_2,E) = i\int \frac{d\omega'}{2\pi}\, e^{-i\delta\omega'} G(\mathbf{r}_1,\mathbf{r}_2,E-\omega')W(\mathbf{r}_1,\mathbf{r}_2,\omega'), \tag{7}$$

where $W(\omega)$ is the screened Coulomb interaction evaluated in the random phase approximation. For more details see, e.g., Refs. 63 and 64. In the simplest implementation of the *GW* approximation, the self-energy is computed non-self-consistently, i.e., by evaluating G and W according to the eigenvalues and eigenvectors of a reference noninteracting Hamiltonian (typically the KS Hamiltonian at the LDA or GGA level). Such a procedure is known as G_0W_0 and gives reasonable results for the QP energies in a number of cases.[63,65,66] In the present paper we exploit the G_0W_0 approximation and evaluate the frequency integrals in Eq. (7) by using a plasmon pole model according to Godby and Needs.[67]

In this work, the main quantities we are interested in are the QP energies. If we neglect finite-lifetime effects and take (or symmetrize) the self-energy to be Hermitian, QP energies are given by first-order perturbation theory as

$$\epsilon_m^{\mathrm{QP}} = \epsilon_m^{\mathrm{KS}} + \langle\psi_m|\,\Sigma\left(\epsilon_m^{\mathrm{QP}}\right) - v_{\mathrm{xc}}\,|\psi_m\rangle. \tag{8}$$

As is customary,[64] in order to solve for ϵ_m^{QP}, the self-energy in the above equation is expanded to first order as a function of E.

In order to gain more physical insight we also refer to the (static) COHSEX[21,64] approximation of *GW*, where the self-energy is written as $\Sigma = \Sigma^{\mathrm{COH}} + \Sigma^{\mathrm{SEX}}$:

$$\Sigma^{\mathrm{SEX}}(\mathbf{r}_1,\mathbf{r}_2) = -\gamma(\mathbf{r}_1,\mathbf{r}_2)\,W(\mathbf{r}_1,\mathbf{r}_2,0), \tag{9}$$

$$\Sigma^{\mathrm{COH}}(\mathbf{r}_1,\mathbf{r}_2) = \tfrac{1}{2}\,\delta(\mathbf{r}_1,\mathbf{r}_2)\,W_p(\mathbf{r}_1,\mathbf{r}_2,0). \tag{10}$$

Here $\gamma(\mathbf{r}_1,\mathbf{r}_2)$ is the one-particle density matrix, and $W_p = W - v$ is the dynamical contribution to W (v being the bare Coulomb interaction). The COHSEX self-energy is thus the sum of a statically screened exchange term and a local potential. This partition is particularly useful for discussing

the connection between hybrid exchange functionals and *GW*. In the former case, the potential can be written as[24]

$$v_{\rm xc}^{\rm hyb} = \alpha\, v_{\rm x}^{\rm NL} + (1-\alpha)\, v_{\rm x}^{\rm L} + v_{\rm c}^{\rm L}, \tag{11}$$

where $v_{\rm x}^{\rm NL}$ is the nonlocal exchange potential, while $v_{\rm x}^{\rm L}$ and $v_{\rm c}^{\rm L}$ are local potentials. It is then straightforward to interpret α as an inverse effective screening to stress the formal analogy of Eqs. (9)–(11). Similar considerations are, of course, valid for more complex forms of hybrid functionals, like range-separated or local formulations.[24,68,69] This formal analogy is well known in the literature,[24] and it has also been further investigated recently.[70] Besides their accuracy for thermochemistry, this analysis highlights that also the electronic structure computed by nonlocal hybrids can benefit from the inclusion of some screened exchange term. Indeed, improved descriptions of the electronic structure for finite and extended systems are typically found,[58,70] even though the accuracy may vary significantly, depending on the system.

B. Interpolation of the *GW* electronic structure using Wannier functions

Dealing with periodic systems, interpolation over the first Brillouin zone (1BZ) is a long standing issue. Calculations are typically performed by discretizing **k** points in the 1BZ, and some postprocessing schemes [e.g., those to compute density-of-states (DOS), Fermi surface, band structure, or phonons] might need a better discretization of the 1BZ than some of the previous steps (often aimed at computing total energy, forces, and charge density). This is particularly critical when the computational requirements of the adopted methods limit the **k**-point discretization, as is the case for *GW* calculations. Schemes able to refine or interpolate[71] over the 1BZ are particularly useful for this purpose. One of these is the *Wannier interpolation*,[31,72–74] where the localization of the WF basis together with the finite range in real space of the Hamiltonian is used to perform a Fourier interpolation of the eigenvalues and, eventually, the eigenvectors. The use of this scheme to interpolate *GW* results has also been reported by Hamann and Vanderbilt.[75]

The procedure can be applied not only to the Hamiltonian but, in principle, to any operator $A(\mathbf{r},\mathbf{r}')$ with the translational symmetry of the Hamiltonian. First, we define the projector P over a subspace of interest,

$$P = \sum_{n\mathbf{k}} |\psi_{n\mathbf{k}}\rangle\langle\psi_{n\mathbf{k}}|, \tag{12}$$

in terms of the eigenvectors of H. When the subspace P is complete, we can represent A as

$$A = \sum_{\mathbf{k}}\sum_{mn} |\psi_{m\mathbf{k}}\rangle\, A_{mn}(\mathbf{k})\, \langle\psi_{n\mathbf{k}}|, \tag{13}$$

$$A_{mn}(\mathbf{k}) = \langle\psi_{m\mathbf{k}}|A|\psi_{n\mathbf{k}}\rangle. \tag{14}$$

Here, A is diagonal with respect to the **k** index because it commutes with the translation operators of the direct lattice (as assumed). In practice, limiting the number of eigenstates of H included in P is equivalent to considering the projection of A on the P subspace, namely, $A^P = PAP$ instead of A. At this point we can use the definition of maximally localized WFs (MLWFs), according to Ref. 73,

$$|w_{i\mathbf{R}}\rangle = \frac{1}{N_{\mathbf{k}}}\sum_{\mathbf{k}} e^{-i\mathbf{k}\mathbf{R}} \sum_{m} U_{mi}^{\mathbf{k}}\, |\psi_{m\mathbf{k}}\rangle, \tag{15}$$

to obtain an expression for the matrix elements of A on the Wannier basis, $A_{ij}^P(\mathbf{R}) = \langle w_{i\mathbf{0}}|A|w_{j\mathbf{R}}\rangle$:

$$A_{ij}^P(\mathbf{R}) = \frac{1}{N_{\mathbf{k}}}\sum_{\mathbf{k}} e^{-i\mathbf{k}\mathbf{R}}\, [U^{\mathbf{k}\dagger} A^P(\mathbf{k}) U^{\mathbf{k}}]_{ij}. \tag{16}$$

Note that when the original Marzari-Vanderbilt procedure[73] is applied without any disentanglement,[74] the $U^{\mathbf{k}}$ matrices are a unitary mapping of N Bloch states (usually, but not necessarily, occupied) into N WFs. Instead, when the disentanglement is performed, the resulting WF set does not span the whole P subspace ($U^{\mathbf{k}}$ are then rectangular matrices). This means that in the general case the final representation of A is actually projected not on P but on the smaller subspace spanned by the WFs.

Assuming that A^P is decaying fast enough in real space to have $\|A^P(\mathbf{R})\| \simeq 0$ for $|\mathbf{R}| > |\mathbf{R}_0|$ (where $\mathbf{R}_0$ is within the finite set compatible with the initial **k**-point grid), we can perform the following Fourier interpolation to obtain the matrix elements of A for any $\mathbf{k}'$ point:

$$A_{ij}^P(\mathbf{k}') = \sum_{\mathbf{R}}^{|\mathbf{R}|<|\mathbf{R}_0|} e^{i\mathbf{k}'\mathbf{R}}\, A_{ij}^P(\mathbf{R}). \tag{17}$$

When interpolating *GW* results, we want to represent the operator $\Sigma(E) = \Sigma^{GW}(E) - v_{\rm xc}$, which is, in general, nonlocal, non-Hermitian, and frequency dependent. For the sake of the Wannier interpolation, we are mainly interested in checking that the intrinsic nonlocality of $P\Sigma P$ is compatible with the selected **k**-point grid (or, in other terms, that the *GW* calculation is converged with respect to the number of **k** points used). The localization of the *GW* self-energy is further discussed in Sec. V A, especially in connection with the usual approximation which neglects off-diagonal $\Sigma_{mn}(\mathbf{k}E)$ matrix elements.

C. Numerical approach

In this work, DFT and hybrid-DFT calculations have been performed using the CRYSTAL09 package.[76] The code implements all-electron electronic structure methods within periodic boundary conditions and adopts an atomic basis set expanded in Gaussian functions (further details in Appendix B). Once the Hamiltonian matrix elements are obtained,[77] the real and CBSs are interpolated (as discussed in the previous sections) using the WANT[30,31] package.

GW results have been obtained using the plane-wave and pseudopotential implementation of SAX,[78] which is interfaced to Quantum ESPRESSO[79] (QE) for DFT calculations. In this case, once the KS electronic structure is evaluated, we first compute MLWFs[73,74] using WANT and then apply the CBS technique. In order to assess any systematic error in comparing *GW* and hybrid-DFT results (which have been obtained using different basis sets such as plane waves and local orbitals), we have also performed hybrid-DFT and HF calculations using QE and SAX. In this case WFs are computed on top of the

already corrected electronic structure. Results are shown for the case of PA [see Table III and Fig. 8 in particular]. The excellent agreement between the two sets of data suggests that the pseudopotential approximation, the basis set, and the numerical thresholds are sufficiently well converged to have negligible influence on the results presented. Full computational details and parameters are reported in Appendix B.

IV. RESULTS

A. Structural properties

Before focusing on the electronic and transport properties of the isolated polymer chains in Fig. 2, we investigate their structure by fully relaxing both the atomic positions and the cell parameters using different exchange-correlation schemes. All systems are treated with one-dimensional periodicity; the details of the calculations (performed using CRYSTAL09) are given in Appendix B. The results for the lattice parameters are reported in Table I.

In the case of PA, electronic properties such as the band gap (as well as the evanescent states) are strongly dependent on the dimerization of the C–C bond lengths (Peierls distortion). Such bond alternation is not easily captured by local and semilocal DFT schemes, leading to band gaps that are far too small, i.e., to an overestimation of the metallicity. Since these parameters are critical to our purpose, we report also the bond length alternation (BLA) for PA in Table I. Our HF results are in excellent agreement with previously published results.[80,81] In the following we label as PA_{HF} the calculations performed using the geometry from Ref. 80, where $c = 2.469$ Å and BLA is 1.339/1.451 Å. We also decided to consider two frozen geometries of PA (namely, PA_1 and PA_2), according to other data in the literature.[8,82] In the case of PA_1[82] we set $c = 2.451$ Å and the BLA to 1.370/1.460 Å, while for PA_2[8] $c = 2.496$ Å and the BLA is 1.340/1.540 Å (assuming ideal C–C bond angles of 120°). In passing, we note that the PA_1 geometry is also very similar to the one adopted in Refs. 83–85, where $c = 2.457$ Å and the BLA is set to 1.360/1.440 Å, according to experimental data.[86,87] Since these theoretical studies report *GW* results, in Sec. IV B we compare them with those for PA_1.

Data from multiple geometries of PA are useful to decouple the electronic and structural effects of the adopted exchange and correlation (XC) schemes on the CBS. Since the extent of this goes beyond PA, in the following we decided to look at the effect of XC treatment first using a frozen geometry, independently of the adopted method, and then to compare them also with the same quantities obtained using fully relaxed geometries. Moreover, since *GW* corrections are usually computed without performing a further structural relaxation, working at fixed geometry allows us to compare *GW* corrections and results from hybrid functionals for identical geometries. For each polymer except PA we adopted the geometry obtained after full relaxation at the PBE level using QE. The lattice parameters (2.564 Å for PE, 6.702 Å for PPV, and 13.004 Å for PPI) are in very good agreement with those in Table I obtained using PBE in CRYSTAL09.

TABLE I. Lattice parameter c (Å) for PA, PE, PPV, and PPI, computed using different XC schemes as implemented in CRYSTAL09. In the case of PA, we also report the bond length alternation (BLA) (Å) of single and double C–C bonds.

Scheme	PA	PA BLA	PE	PPV	PPI
LDA	2.463	1.369/1.416	2.537	6.644	12.869
PW	2.482	1.376/1.428	2.570	6.712	13.001
BLYP	2.493	1.380/1.435	2.590	6.747	13.079
PBE	2.484	1.378/1.429	2.572	6.719	13.014
B3PW	2.471	1.362/1.432	2.560	6.692	12.961
B3LYP	2.476	1.375/1.435	2.570	6.706	12.998
PBE0	2.468	1.359/1.432	2.553	6.680	12.938
HF	2.465	1.332/1.457	2.556	6.689	12.950

B. Electronic structure: Polyethylene and polyacetylene

In this section we investigate the effect of different XC schemes (local and semilocal DFT, hybrid functionals, HF, and *GW*) on the electronic properties of two prototype polymers (PE and PA), while results for PPV and PPI are reported in Sec. IV C. We compute both the real and the CBSs. Figures 3 and 4 refer to the case of frozen geometries (i.e., geometry is not changing according to the adopted scheme; see also Sec. IV A). Details on the electronic structure of the three PA geometries studied are reported in Table III. In the case of PA (as well as PPV), we can also compare the results with previously published *GW* calculations.[83–85,88] Note that the *GW* results are interpolated using MLWFs, which results in filtering out some of the states above the vacuum level.

In Fig. 3, we report[77] the real and CBSs for PE. Our results are in reasonably good agreement with previously published

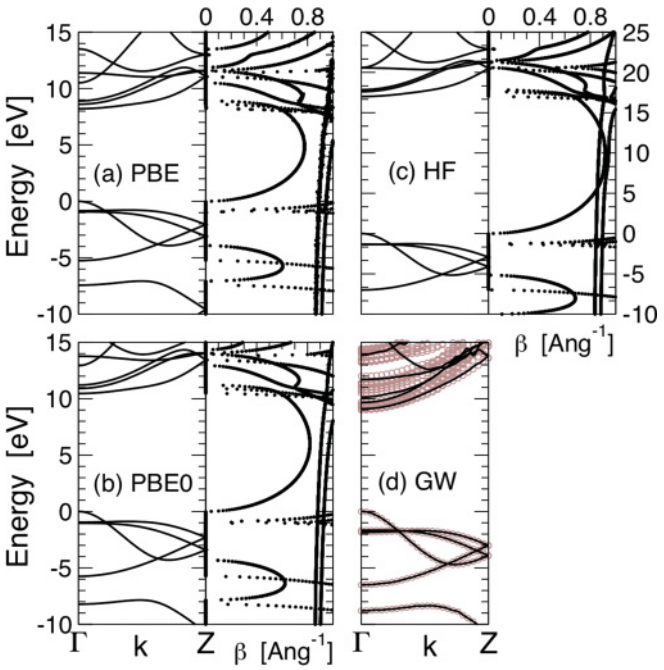

FIG. 3. (Color online) Polyethylene. Real and complex band structures using the following schemes: (a) PBE, (b) PBE0, (c) HF, and (d) *GW*. Solid (black) lines in (a)–(c) refer to CRYSTAL09 calculations. *GW* results were obtained using SAX (circles) and interpolated with WFs [solid (black) lines].

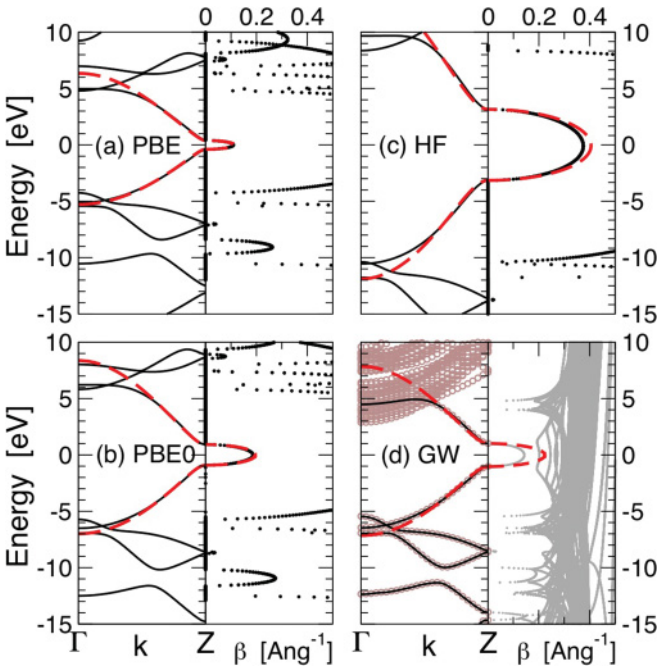

FIG. 4. (Color online) Polyacetylene (PA_1 geometry). Real and complex band structures using the following schemes: (a) PBE, (b) PBE0, (c) HF, and (d) *GW*. Solid (black) lines in (a)–(c) refer to CRYSTAL09 calculations. *GW* results were obtained using SAX (circles) and interpolated with WFs [solid (black) lines]. Dashed (red) lines refer to data interpolated according to the tight-binding model in Appendix A.

theoretical data.[8,10,19,89,90] As shown in Figs. 3(a) and 3(b), the maximum value of β from the arc across the fundamental gap does not change much when passing from PBE to PBE0 ($\beta_{\max} \simeq 0.8$ Å^{-1}). In agreement with Ref. 10, we believe this to be one of the reasons why the β values computed at the LDA or GGA levels were found to be in agreement with the experiment.

The main qualitative difference from Fig. 2(a) in Ref. 19 comes from the filtering of some vacuum-like states, due to the use of the localized basis (or WF interpolation) in our approach. Our results are more similar to those presented in Ref. 8, obtained using a localized basis set. This has little influence on the part of the CBS spectrum that is physically relevant for the nonresonant tunneling experiment. The G_0W_0-corrected band structure is reported in Fig. 3(d). The G_0W_0 CBS is not computed here because the missing self-consistency is critical for the CBS, as discussed in Sec. V A. Instead, we have computed CBS from the self-consistent[91] COHSEX electronic structure. All results for $\beta_{\max}$ are collected in Table II, where we compare data obtained using CRYSTAL09 versus QE or SAX after Wannierization. Results and trends compare reasonably well.

In Fig. 4, we show the results for the real and CBSs in the case of PA_1. The dependence of the β parameter on the exchange-correlation scheme is displayed. As expected, upon increasing the percentage of nonlocal exchange from PBE (0%), to PBE0 (25%), up to HF (100%), the band gap opens, and the "degree of localization" increases as indicated by the increasing values of $\beta_{\max}$. This trend is general and also found for the other conjugated polymers studied in this work. A detailed description of the computed band structure for PA in the PA_{HF}, PA_1, and PA_2 geometries is reported in Table III for all the methods.

In order to gain more physical insight from our calculations, we have also fitted the data using the generalized

TABLE II. Polyethylene: Maximum $\beta(E)$ (Å^{-1}) inside the gap computed by means of different theoretical schemes. Results were obtained by CRYSTAL09 (CRY) and by Quantum ESPRESSO (QE)–SAX.

	Polyethylene				
$\beta_{\max}$	LDA	PBE	PBE0	HF	COHSEX
CRY	0.77	0.77	0.81	0.92	
QE-SAX	0.80	0.81		0.94	0.94

TABLE III. Polyacetylene $(PA)_{HF}$, PA_1, and PA_2: Band gap (E_g; in eV), hopping parameters (t_1, t_2; in eV) according to the tight-binding (TB) model in Eq. (A5), and maximum $\beta(E)$ (Å^{-1}) inside the gap. Calculations were performed using DFT, hybrid-DFT, HF, and diagonal-*GW* schemes. $\beta_{\max}$ values through the CBS interpolation, using the TB model, are also listed. All data were computed using CRYSTAL09 except the *GW* results and the X-QE lines (X = LDA, PBE, PBE0).

Scheme	E_g	t_1	t_2	$\beta_{\max}$	$\beta_{\max}^{\text{model}}$
			PA_{HF}		
LDA	0.99	2.97	0.199	0.13	0.13
PW	1.01	2.97	0.203	0.14	0.14
BLYP	1.02	2.96	0.199	0.14	0.14
PBE	1.01	2.98	0.204	0.14	0.14
B3PW	1.94	3.78	0.223	0.19	0.21
B3LYP	1.95	3.77	0.218	0.20	0.21
PBE0	2.20	3.98	0.228	0.21	0.22
HF	6.97	6.45	0.277	0.38	0.43
d-G_0W_0	2.60	3.85	0.154	(0.17)	0.27
LDA-QE	0.99	3.02	0.214	0.13	0.13
PBE-QE	1.02	3.00	0.212	0.14	0.14
PBE0-QE	2.22	3.99	0.238	0.20	0.22
			PA_1		
LDA	0.78	2.90	0.144	0.11	0.11
PW	0.80	2.90	0.148	0.11	0.11
BLYP	0.80	2.89	0.144	0.11	0.11
PBE	0.80	2.91	0.149	0.11	0.11
B3PW	1.64	3.73	0.166	0.17	0.18
B3LYP	1.64	3.72	0.161	0.17	0.18
PBE0	1.88	3.94	0.171	0.18	0.19
HF	6.46	6.46	0.212	0.36	0.40
d-G_0W_0	2.05	3.72	0.090	(0.14)	0.22
			PA_2		
LDA	1.68	2.76	0.134	0.24	0.24
PW	1.72	2.76	0.139	0.25	0.25
BLYP	1.72	2.75	0.134	0.25	0.25
PBE	1.72	2.77	0.139	0.25	0.25
B3PW	2.89	3.49	0.153	0.31	0.33
B3LYP	2.90	3.47	0.149	0.31	0.33
PBE0	3.20	3.67	0.158	0.33	0.35
HF	8.37	5.88	0.196	0.50	0.56
d-G_0W_0	4.17	3.87	0.092	(0.27)	0.43

nearest-neighbor (NN) model presented in Sec. II and Appendix A. This model has three parameters, which approximately correspond to the band gap E_g and the band widths of the HOMO and LUMO bands (related to the parameters t_1 and t_2). The proper relation between the band widths and $t_{1,2}$ is given in Eqs. (A11) and (A12). The main difference between this model and the one introduced in Ref. 8 is that the one used here allows for different band widths for the HOMO and LUMO. While this difference is found to be small (but generally not negligible) in the cases studied, the generalized model allows for a more accurate fitting of the electronic structure of polymers. As shown in Figs. 4(a)–4(c), the model fitting [dashed (red) lines] is very accurate for all the local, semilocal, and hybrid functionals. In general, the HF data show the largest deviation from the model. We believe the nonlocal nature of the exchange potential to be the origin of this behavior.

Figure 4(d) reports the *GW* results for PA_1. The fundamental gap is 0.8 eV at the PBE KS-DFT level, while it increases to 2.05 eV when G_0W_0 is applied. This is in very good agreement with previous *GW* data for PA.[83–85,92] As already mentioned, *GW* calculations are performed by using plane waves and pseudopotentials, while the hybrid-DFT is evaluated on a localized basis set. In order to assess a possible systematic error due to this procedure, we have also computed the electronic structure of PA_{HF} at the LDA, PBE, and PBE0 levels, by using the plane-wave implementation of QE. Results are reported in Table III on the "X-QE" rows (X = LDA, PBE, PBE0). The two sets of data are found to be in excellent agreement, allowing for a direct comparison of *GW* and hybrid-DFT data. See also Sec. V A and Fig. 8(b) for further details.

As a last remark, according to the standard approach for *GW* calculations,[63,64] only the KS eigenvalues are corrected, without modifying the wave functions. In other words, only the diagonal matrix elements of the self-energy (on the original DFT Bloch eigenvectors) are considered. The effects of this are analyzed in detail in Sec. V A, where it is demonstrated that this procedure has a sizable effect on the calculation of the CBS. For this reason, the *GW* CBS directly computed is reported in a lighter color in the right panel in Fig. 4(d), while β_{max} is listed in parentheses in Table III.

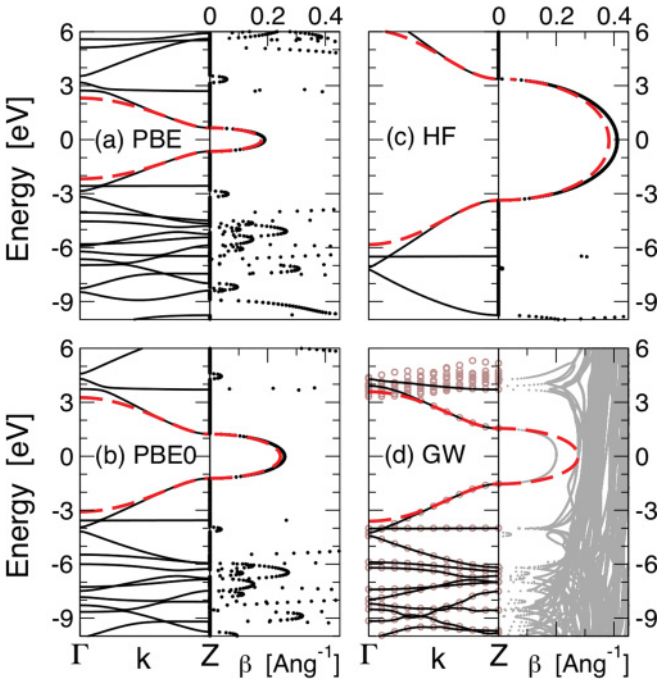

FIG. 5. (Color online) PPV: Real and complex band structures, as in Fig. 4.

TABLE IV. Poly-(*para*-phenylene-vinylene) (PPV): Band gap (E_g; eV), hopping parameters (t_1, t_2; eV), and maximum $\beta(E)$ (Å^{-1}) inside the gap (computed and fitted from the tight-binding model), as in Table III. The last column reports the β_{max} values for the relaxed geometries.

Scheme	E_g	t_1	t_2	β_{max}	β_{max}^{model}	β_{max}^{relax}
LDA	1.28	1.07	0.016	0.19	0.18	0.18
PW	1.31	1.07	0.017	0.19	0.18	0.19
BLYP	1.31	1.07	0.016	0.19	0.18	0.19
PBE	1.31	1.07	0.017	0.19	0.18	0.19
B3PW	2.22	1.39	0.021	0.25	0.23	0.26
B3LYP	2.22	1.38	0.020	0.25	0.23	0.26
PBE0	2.46	1.46	0.022	0.26	0.24	0.28
HF	6.74	2.46	0.033	0.41	0.38	0.46
G_0W_0	3.09	1.63	−0.004	0.20(d)	0.28	

C. Electronic structure: PPV and PPI

In this section we consider two further polymers, namely, PPV and PPI. PPV has been largely investigated for its role in organic (opto-)electronics,[25] while oligo-(phenylene-imine) molecules attached to gold leads have recently been considered and the β-decay coefficents measured.[7,26] This makes these two polymers particularly appealing for our analysis.

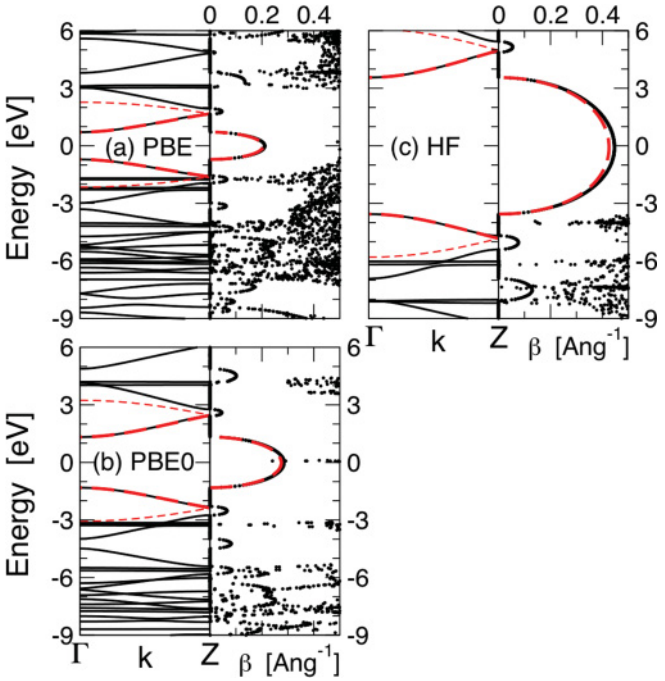

FIG. 6. (Color online) PPI: Real and complex band structures, as in Fig. 4. The fitting procedure was applied on a cell of half-length and then folded, resulting in four bands instead of two.

TABLE V. Poly-(phenylene-imine): Band gap (E_g; in eV), hopping parameters (t_1, t_2; in eV), and maximum $\beta(E)$ (Å^{-1}) inside the gap (computed and fitted from the tight-binding model), as in Table III. The last column reports the $\beta_{\max}$ values for the relaxed geometries.

Scheme	E_g	t_1	t_2	$\beta_{\max}$	$\beta_{\max}^{\text{model}}$	$\beta_{\max}^{\text{relax}}$
LDA	1.40	1.05	0.014	0.21	0.20	0.20
PW	1.42	1.05	0.014	0.21	0.20	0.21
BLYP	1.42	1.04	0.014	0.21	0.21	0.21
PBE	1.42	1.05	0.014	0.21	0.20	0.21
B3PW	2.38	1.36	0.020	0.27	0.26	0.29
B3LYP	2.38	1.35	0.019	0.27	0.26	0.29
PBE0	2.64	1.43	0.021	0.29	0.28	0.30
HF	7.12	2.38	0.036	0.45	0.43	0.50

Results for PPV are reported in Fig. 5 and Table IV. The behavior of the real and CBSs are qualitatively in agreement with what we have found for PA. PBE0 results ($\beta_{\max} = 0.26$ Å^{-1}) are those among the hybrid functionals that best compare with the interpolated *GW* data ($\beta_{\max} = 0.28$ Å^{-1}), though slightly underestimating $\beta_{\max}$ and, to a larger extent, the band gap. In the case of PPI, results are reported in Fig. 6 and Table V. For this polymer, the model fitting has been applied on a cell of half-length and then bands have been folded, leading to four interpolated bands instead of two. Despite the reduction of translational symmetry, this procedure leads to a better fit because it describes a larger part of the frontier electronic structure. In agreement with previous cases, while we do not have *GW* results for PPI, we consider PBE0 data ($\beta_{\max}^{\text{relax}} = 0.29$ Å^{-1}) as our best estimate. In the next section we also discuss the comparison of these computed data with recent experimental results.[7,26] For the PPV and PPI cases, we have also studied separately the effect of the geometrical relaxation induced by the different functionals on the CBS. This effect is consistent with the trends already observed at fixed geometry. In the last columns in Tables IV and V we report the $\beta_{\max}$ value for the relaxed polymer geometries (labeled $\beta_{\max}^{\text{relax}}$). The $\beta_{\max}$ parameters increase further with increasing fraction of nonlocal exchange, when the geometries are relaxed according to the adopted functional. While the coupling of the electronic structure with the structural properties is particularly evident and critical in the case of PA (since the opening of the gap is due to Peierls distortion of the C–C bonds), it is much less pronounced for PPV and PPI, where it accounts for a correction term only, the leading contribution being the description of the electronic levels.

V. DISCUSSION

A. Analysis of the *GW* data

In this section we discuss the effect of some of the approximations involved in the evaluation of the *GW* self-energy. In particular, we address issues related to the representation of Σ when computing the CBS, as well as the effect of the self-consistency. The *GW* self-consistency is investigated within the static COHSEX approximation. In doing so, we discuss the localization properties of the resulting Hamiltonians together with the quality of the NN model fitting of the CBS. We focus on the case of PA, which is a good prototype for this class of one-dimensional systems.

Let us begin with the representation problem. As already recalled in Sec. III B, assuming a large enough subset of Bloch vectors (in principle, all of them), the self-energy operator can be represented as

$$\Sigma^{GW}(E) = \sum_{\mathbf{k}} \sum_{mn} |\psi_{m\mathbf{k}}\rangle \, \Sigma_{mn}(\mathbf{k}\, E) \, \langle \psi_{n\mathbf{k}}| \qquad (18)$$

[see also Eqs. (13) and (14)]. In the usual *GW* practice, besides evaluating the self-energy by using the underlying KS-DFT electronic structure for G and W (G_0W_0 approximation, i.e., no self-consistency), it is also customary to neglect the off-diagonal band indexes $m \neq n$ in Eq. (18) when computing QP energies. This approximation forces the self-energy to be diagonal on the KS-DFT Bloch states and, thus, allows us to modify the QP energies without changing the DFT wave functions. If we assume that the correctly represented self-energy Eq. (18) is physically short-ranged in real space (further comments follow), as happens, e.g., for HF and COHSEX, when the representation is taken to be diagonal on the Bloch basis, spurious long-range components of the self-energy may (and typically do) arise. The diagonal approximation has been found[64] to have little effect on the QP energy spectrum (at least when LDA wave functions are a reasonable starting point). Our investigations confirm this picture at both the HF and the COHSEX level. As discussed in the following, the case of the CBS is more critical.

First, we focus on a tight-binding model. In Fig. 7 we report the real and complex band structures for such a model, according to Appendix A. In order to simulate the effect of a diagonal self-energy, we refer to a picture where the Σ correction can be modeled as a stretching of the bands (which may be different for valence and conduction states)

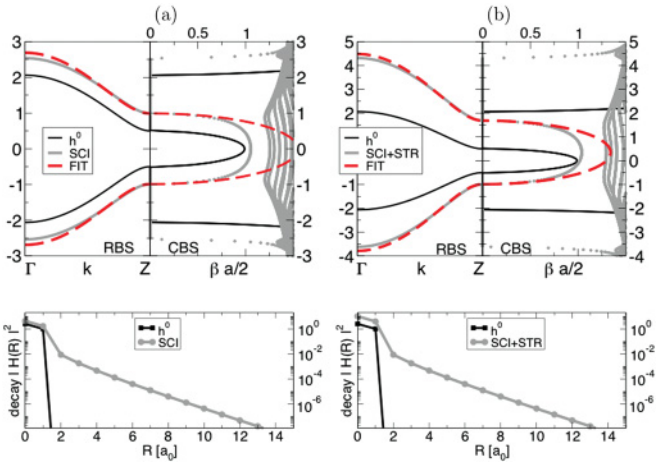

FIG. 7. (Color online) Real and complex band structures for a nearest-neighbor (NN) tight-binding model Hamiltonian h^0 [thin solid (black) line]. Scissor (a) and scissor + stretching (b) corrections to h^0 are applied. Thick solid (gray) lines represent the electronic structures obtained while including such corrections. Dashed (red) lines are obtained by an NN tight-binding fitting of the real electronic structure after corrections. Lower panels report the spatial decay of the original and corrected Hamiltonians.

plus a scissor operator applied to the HOMO-LUMO gap. A simple scissor [Fig. 7(a)] and a scissor + stretching [Fig. 7(b)] correction are applied to the model in Fig. 7 [solid (black) lines for the original model, thick solid (gray) lines for the corrected ones]. The new Hamiltonian including the corrections is now longer-range than the original NN Hamiltonian h^0, because of the nonlocal projectors used to express the scissor and scissor + stretching corrections. The different spatial decay of the pristine and corrected Hamiltonians is shown in the lower panels in Fig. 7. We then fit the corrected Hamiltonian by again using the NN model [dashed (red) lines]. This fitting emulates the real band structure, but using a short-range (NN) Hamiltonian. The effect on the CBS is evident and sizable. The simply shifted and stretched electronic structures leads to small corrections to the CBS, while much larger corrections are obtained when considering the fitted short-range Hamiltonians. Because CBS measures the decay of the evanescent states in real space, it is not surprising that a method which does not update the wave functions (as the diagonal self-energy corrections) is not able to capture all of the physics involved in the change of the electronic structure.

In order to further numerically support this interpretation and to investigate the effect of the self-consistency, we evaluated the HF and COHSEX self-energies for PA_{HF}. At first we did so non-self-consistently (self-energies evaluated on the LDA wave functions), with and without the diagonal approximation. Then self-consistent[91] COHSEX results are provided. HF results are plotted in Figs. 8(a) and 8(b); COHSEX data, in Fig. 8(c). LDA β_{max} is shown by a dashed line in the CBS panels as a reference. Regarding the real band structure, we found that the inclusion of off-diagonal matrix elements is not very relevant for PA, the bands being almost overlapping for both HF and COHSEX [diagonal data shown in Figs. 8(a) and 8(c) by dashed (gray) lines]. The situation is different for the CBS, as is highlighted in Fig. 8(a). The HF_0 correction of β_{max} from the full off-diagonal representation is almost twice as large as the diagonal correction. This confirms the behavior observed with the models in Fig. 7.

This observation also correlates with the decay of the HF_0 (LDA) Hamiltonian reported in the lower part of Fig. 8(a). As for the models (Fig. 7), the diagonal representation induces a much longer (and unphysical) decay. The same situation is found for COHSEX (the off-diagonal results at the first SCF iteration are not shown). The proper Hamiltonian decay (black line with circles) is clearly longer-range than the LDA results, because of the nonlocal contribution of the exchange operator. The decay of the exchange potential is driven by that of the density matrix, which in turn is related[29] to β at the branch point. As β_{max} is typically underestimated at the LDA level, so is the decay of the HF_0 Hamiltonian. The effect of the self-consistency of HF (as well as COHSEX) is then to reduce such over-delocalization and to produce shorter-range self-energies. This is shown in the decay plot in Figs. 8(b) and 8(c).

This behavior has strong consequences regarding the quality of the NN model fit. In the case of local and self-consistent hybrid functional calculations from CRYSTAL09, the model fit [dashed (red) lines in Figs. 4 and 5] works very well compared with the full calculations, despite its simplicity. This is not the case in comparison with the diagonal corrections in

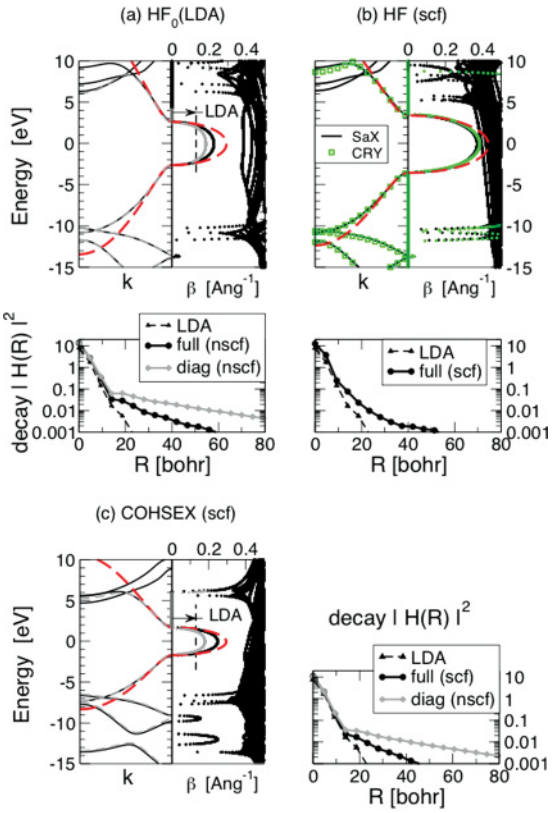

FIG. 8. (Color online) Real and complex band structures for PA_{HF} at the HF and COHSEX levels. (a) Non-self-consistent HF results with a diagonal [solid (gray) lines] and fully off-diagonal (black lines) representation of the correction. (b) The same data for the self-consistent HF solution, as computed from SAX [solid (black) lines] and CRYSTAL09 [(green) triangles]. (c) COHSEX data: Diagonal non-self-consistent [solid (gray) lines] and fully self-consistent [solid (black) lines] data are reported. In both cases, an NN tight-binding fit of the real and complex band structures is performed [dashed (red) lines]. Lower panels show a measure of the spatial decay of the COHSEX and HF Hamiltonian matrices on the WF basis.

Figs. 8(a) and 8(c). The off-diagonal representation improves the situation but does not solve the problem. The failure of the model fit in Fig. 8(a) is in fact mostly related to the decay of the exchange operator. A much better fit is then found when full self-consistency is included, as in Figs. 8(b) and 8(c). Finally, we have also compared the HF results from SaX (plane waves and pseudopotentials) and CRYSTAL09 (localized basis, full electron). Results are reported in Fig. 8(b) by the solid (black) lines and the (green) triangles, respectively. We find excellent agreement for both the real and the CBSs, confirming that the results from the two codes are well comparable and free of any systematic error.

In light of the discussion above, when presenting the diagonal G_0W_0 data for PA and PPV [Figs. 4(d) and 5(d)], the CBS is better described by the interpolated data (dashed lines) instead of the data directly calculated from the diagonal *GW* corrections (thin solid lines). Similar conclusions about the importance of describing changes to wave functions when applying *GW* to transport calculations are also reported in Refs. 49, 50, and 93.

B. Electronic structure

Now we can turn to a discussion of the accuracy of the electronic structure calculations for conjugated polymers. First, we note that our results for PA_1 and PPV are in good agreement with previously published[83–85,92] G_0W_0 results. In particular, for PA_1 we obtain a *GW* gap $E_g = 2.05$ eV, to be compared with 2.1 eV[83,85] and 2.13 eV.[92] These results are obtained for isolated chains of PA. In the case of a crystal, the gap shrinks[84] to 1.8 eV due to interchain interactions. For the isolated chain of PPV, Rohlfing *et al.*[83,85] found $E_g = 3.3$ eV (G_0W_0), which compares reasonably well with our G_0W_0 result of 3.09 eV (see Table IV). In general, the overall shape (including the band widths) of the GW-corrected band structures for PA and PPV computed in this work is in excellent agreement with that of Ref. 85.

From a methodological point of view, the accuracy of G_0W_0 corrections (based on the LDA electronic structure) for organic molecules has been recently widely addressed,[59,62,94–96] compared with different implementations of self-consistent *GW* and experimental results. G_0W_0 (LDA) is found to underestimate ionization potentials more than in extended systems, suggesting that a certain degree of self-consistency tends to improve on the results. Moreover, self-consistency is found to further lower the HOMO level and increase the fundamental gap. This leads to larger estimates of $\beta_{\max}$.

In terms of a direct quantitative comparison with experiments, some issues have to be taken into account. First, the electronic structure (and optical) measurements for polymers typically distinguish between crystalline grains and amorphous regions. Isolated chains are considered to resemble more (and to be used as rough models for) the amorphous regions. Clearly, a direct theory-experiment comparison may suffer from systematic errors (interchain interactions, medium polarization, electrostatic effects). These features generally tend to reduce the fundamental gap with regard to that of the ideally isolated chain. With this in mind, we can compare data calculated here with experimental data from photoemission or scanning tunneling spectroscopy (STS). Rinaldi *et al.* measured[97] the electronic gap of PPV films (on a GaAs substrate) by means of STS. They were able to estimate $E_g \sim 3$ eV. Kemerik*et al.*[98] also used STS and found the fundamental gap of PPV [film deposited on Au(111)] to be around 2.8 eV. All of these results are to be reasonably considered as lower bounds of the theoretical gap for the isolated PPV chain.

C. Complex band structure: Trends

As can be directly inferred from the model described in Appendix A, as well as from Ref. 8, the important parameters that determine the behavior of $\beta(E)$ (and $\beta_{\max}$) are the band gap E_g and the effective band widths of the states around the gap, given, e.g., in terms of the hopping t_1. While our model (see Appendix A) includes a second parameter t_2 to describe the difference in the band widths of the frontier bands, considering that the ratio t_2/t_1 ranges from 0.1 to 0.01 or less, corrections to the model due to t_2 are not particularly relevant for the cases studied here. According to Eqs. (A4) and (A18), $\beta_{\max}$ is mostly determined by the E_g/t_1 ratio. Even though this is just a simplified NN model, our numerical investigations suggest that the model is widely applicable (using a folding technique as in the case of PPI when needed).

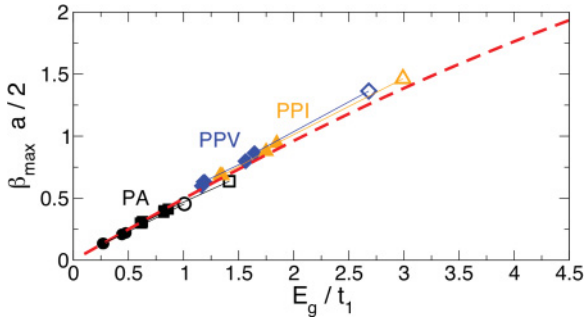

FIG. 9. (Color online) Computed $\beta_{\max}\, a/2$ versus E_g/t_1, E_g being the band gap, t_1 the effective hopping, and a the lattice parameter. All polymers and XC functionals or methods are plotted. Filled (black) circles, PA_1; filled (black) squares, PA_2; filled (blue) diamonds, PPV; filled (orange) triangles, PPI. Open symbols refer to HF results. Dashed (red) line: $\beta_{\max}$ according to the tight-binding model.

In general the band gaps are expected to increase with the fraction of nonlocal exchange included in the hybrid functional. For covalently bonded systems, the same trend is expected for the band widths. Numerically, in all our examples, while increasing the energy gap, HF increases also the band widths. The same trend is found for all the hybrid functionals we have investigated. Since both E_g and t_1 increase, it is not trivial to understand *a priori* which mechanisms would dominate. Indeed, it is very clear that the band gap opens more than the band width, leading to a clear trend of $\beta_{\max}$ increasing when a larger fraction of exchange is included in the calculation. The same trend is also found for the *GW* results, even though we had to extrapolate the CBS from the real band structure by using the model fitting (as described in detail in Sec. V A).

In Fig. 9 we report a synthetic view of all the computed values of $\beta_{\max}$ (times $a/2$, a being the polymer lattice parameter), including all electronic structure methods for PA (PA_1 and PA_2 are shown; PA_{HF} is not shown because it is almost superimposed on the other PA geometries), PPV, and PPI. These data are plotted against the E_g/t_1 value. The ideal curve from the tight-binding NN model is reported [dashed (red) line]. The agreement between the computed and the modeled data is remarkable for all the cases studied. HF data are represented by open symbols, showing, in general, a slightly worse agreement (as discussed in Sec. IV C). On the basis of the above relations, and according to the results reported in Fig. 9, we suggest the use of the model fitting to extrapolate information about $\beta_{\max}$ from experiments able to investigate the electronic structure. This would allow for an indirect measure of the CBS and the related parameters (as $\beta_{\max}$).

D. Comparison with transport data

As discussed in Secs. I and II, in order to compute the β decay of the current (or conductance) in a MIM junction, we need two ingredients: (i) knowledge of the CBS for the infinitely long insulating region and (ii) the position of the

Fermi level of the MIM junction with regard to the band structure of the insulator. This is depicted in Fig. 1. Assuming that at low bias the current is carried by the states close to the Fermi level of the junction, we basically need to know how these states decay into the insulating region (the polymer, in the present case). Once the CBS is known, either the Fermi level alignment is computed explicitly or it is estimated on the basis of physical considerations. While the direct calculation is feasible (but demanding), and in some cases necessary, it is also possible to give a first estimate of the Fermi level according to the so-called MIGS theory.[8,27,99] As proposed by Tersoff,[27] if the metal DOS around the Fermi level is sufficiently featureless and the MIGSs penetrate deep enough in the insulating region, the Fermi level of the metal-insulator junction is approximately pinned at the charge-neutrality level (often close to the midgap point) in order to avoid charge imbalance at the interface. The charge neutrality level can be easily identified from the CBS, as the energy where $\beta(E)$ reaches its maximum inside the gap. From this perspective, $\beta_{\max}$ is the first estimate of the experimental β decay. In general, the Fermi level will move from the charge neutrality level and the β decay will change accordingly. The physical reasons leading the Fermi level to shift are mostly related to the charge transfer (and dipole formation) at the interface. This explains why different chemical linking groups on the same molecule may lead to different values of β. In general, the $\beta_{\max}$ value computed from the CBS may be regarded as an upper bound for β and thus as a lower bound for the ability of the insulating layer to allow the current to tunnel through the junction.

The above discussion stresses the fact that the experimentally measured β does not, in general, depend[8] only on the electronic structure of the insulator (especially the CBS), but also on the details of the interface (which determines the position of the Fermi level). For instance, recent measurements on alkanes (oligomers of PE) determined a β-decay length of 0.71–0.76 Å^{-1} for $-NH_2$ terminations,[100–102] while it has been found in the range 0.8–0.9 Å^{-1} (and more disperse) for thiolated molecules.[5,102–104] Recent calculations confirm this picture also for conjugated polymers connected to gold leads through different chemical groups.[9] In that work, the authors have studied a number of oligomers including oligophenylenes (whose infinite polymer is PPP). In the case of the molecule connected to gold leads via thiol groups, after investigating the interface-DOS projected on the molecule, they find that the Fermi level aligns close to the midgap point (reasonably the charge neutrality level considered here), off by a few tenths of electron volts (∼0.2–0.3 eV, the molecular gap being about 2 eV) at the LDA level. Since the basic unit of PPP (a phenyl ring) is the same as part of the monomers forming PPV and PPI, we assume the charge neutrality condition to be almost fulfilled if we were considering Au-PPV-Au and Au-PPI-Au junctions with thiol anchoring. We can thus estimate $\beta_{\max}$ to be a good estimate of β, keeping in mind that a small deviation from the midgap would slightly decrease β.

Recent experiments[7,26] reported $\beta = 0.3$ Å^{-1} for oligomers of PPI connected to the gold substrate through a thiol group. This number is in very good agreement with the value $\beta_{\max} = 0.29$ Å^{-1} we found for PPI using PBE0 (see Table V). According to our findings for PA and PPV (see Tables III and IV), *GW* should give results for β comparable to PBE0, but slightly larger. In order to compare with other existing (experimental and theoretical) results for oligophenylenes (PPP in the infinite limit),[23,103,105,106] we would need to address separately the issue of the Fermi level alignment (tending to decrease β with regard to the ideal $\beta_{\max}$) and that of the phenyl twist angle (which goes in the direction of increasing β). This will be the subject of future work. Coming to the case of PA, we note that recent experimental results[107,108] report β values of 0.22 Å^{-1} for molecules similar to oligoacetylenes. While this number is in very good agreement with our *GW* (and PBE0) results for PA_1 (and consistent with PA_{HF}; see Table III), the large variability of β with the structural parameters of PA does not allow us to be conclusive on the assessment of the theory vs the experiment for this specific case. Nevertheless, our findings suggest that the use of PBE0 or *GW* results, together with proper determination of the Fermi level alignment, will provide a reasonable approximation. We also note that gap underestimation and *a priori* assumption of the validity of the MIGS theory tend to partly cancel each other, and fortuitous agreement of experimentally measured β values with LDA calculations may occur.

VI. CONCLUSIONS

In this work we have computed from first principles the real and CBSs of prototype alkylic and conjugated polymer chains using a number of theoretical schemes, ranging from local and semilocal to hybrid-DFT and *GW* corrections. The accuracy of these different methods has been evaluated and compared with existing theoretical and experimental data, in terms of both the electronic structure and the transport properties. From the CBS the β-decay parameter, which governs nonresonant tunneling experiments through MIM junctions, can be computed.

In doing so, we have stressed the formal analogy of hybrid-DFT and *GW* (especially in the COHSEX formulation) and the interpretation of the hybrid-DFT electronic structure as an approximation to the proper QP spectrum. We have also described in detail how to interpolate *GW* results using a WF scheme. In this case we have found that while the real band structure is always well interpolated, the CBS needs the self-energy real-space decay to be properly treated (off-diagonal representation and self-consistency of the wave functions).

We have numerically investigated four polymers, namely, PE, PA, PPV, and PPI. Our results compare well with the existing theoretical and experimental literature. Among the hybrid functionals studied, PBE0 results compare best with the G_0W_0 electronic structure. While the PBE0 band gaps may still have a non-negligible deviation from *GW*, the agreement is remarkable on the CBS and β coefficient. The comparison with transport data (when available) is also very promising. This suggests PBE0 as an efficient and reliable alternative to *GW* for these class systems, at least for transport properties. More generally, a systematic application of hybrid functionals to improve the accuracy of DFT-based electronic structure results is appealing, while further developments along the lines of Ref. 70 are probably needed.

APPENDIX A: ONE-DIMENSIONAL MODEL

In the case of one-dimensional systems like conjugated polymers, numerical results for β can be rationalized in terms

of a simple tight-binding model as presented in Ref. 8. In their work, Tomfohr and Sankey presented a two-band model which provides an analytical expression for the CBS within the fundamental energy gap. This model can also be used to fit the real band structure of realistic systems in order to evaluate the CBS analytically. The model is described in terms of two inequivalent sites ($\epsilon_{a,b}$) with NNs hopping t_1. These three parameters can be recast into E_g (the fundamental gap), t_1, and a further shift of the energy levels, which has no physical meaning. Moreover, it is shown that in this case $\beta_{\max}$ [the maximum value of $\beta(E)$ within the fundamental gap] depends only on E_g/t_1, according to

$$\beta(E)a/2 = \ln[\gamma(\mathrm{E}) + \sqrt{\gamma(\mathrm{E})^2 - 1}], \tag{A1}$$

$$\gamma(E) = \frac{(E - E_v)(E_c - E)}{2t_1^2} + 1, \tag{A2}$$

$$E_{\beta_{\max}} = \Sigma = \frac{E_v + E_c}{2}, \tag{A3}$$

$$\gamma(E_{\beta_{\max}}) = 1 + \frac{1}{8}\left(\frac{E_g}{t_1}\right)^2. \tag{A4}$$

All the details are given in Ref. 8. We note, however, that this model is unable to reproduce any difference in the widths of the two bands (thus resulting in the CBS maximum being located at midgap), while in our realistic simulations we typically find the LUMO band width to be somewhat greater than that of the HOMO. We have then generalized the above to the following three-parameters model, which is more suitable for determination of the relevant physical quantities from our simulations. Extending the previous model, we add second-NN interactions (with strength t_2) between equivalent sites, t_1 being the hopping between inequivalent sites as in the previous model. The model Hamiltonian is

$$\begin{aligned} H = &\sum_{\mathbf{R}} \epsilon_a \psi^\dagger_{a,\mathbf{R}} \psi_{a,\mathbf{R}} + \sum_{\mathbf{R}} \epsilon_b \psi^\dagger_{b,\mathbf{R}} \psi_{b,\mathbf{R}} \\ &+ \sum_{\mathbf{R}} t_1 [\psi^\dagger_{a,\mathbf{R}} \psi_{b,\mathbf{R}} + \psi^\dagger_{a,\mathbf{R}+1} \psi_{b,\mathbf{R}}] + \text{c.c.} \\ &+ \sum_{\mathbf{R}} t_2 [\psi^\dagger_{a,\mathbf{R}+1} \psi_{a,\mathbf{R}} + \psi^\dagger_{b,\mathbf{R}+1} \psi_{b,\mathbf{R}}] + \text{c.c.}, \end{aligned} \tag{A5}$$

where a,b indicate inequivalent sites and R is a cell index. The model is pictorially described in Fig. 10. The parameters t_1 and t_2 are, in general, complex numbers. Taking t_1 and t_2 to be real, for simplicity, the analytical expressions of the energy bands read

$$E_{1,2}(k) = \Sigma + 2t_2\, x(k) \pm \left[\Delta^2 + 2t_1^2\, x(k)\right]^{\frac{1}{2}}, \tag{A6}$$

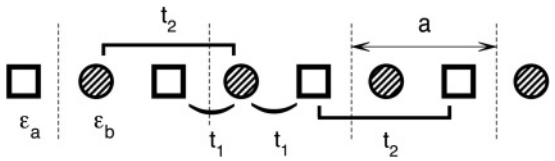

FIG. 10. Scheme of the Hamiltonian adopted to fit the computed data, according to Eq. (A5).

where, assuming $\epsilon_a > \epsilon_b$, we have set

$$E_v = \epsilon_b - 2t_2, \quad E_c = \epsilon_a - 2t_2, \tag{A7}$$

$$x(k) = 1 + \cos(ka), \tag{A8}$$

$$\Sigma = \frac{1}{2}(E_c + E_v), \tag{A9}$$

$$\Delta = \frac{1}{2}(E_c - E_v) = \frac{E_g}{2}. \tag{A10}$$

In this picture $E_{c,v}$ are the onsets of the valence and conduction bands, a is the lattice parameter, and k runs from $-\frac{\pi}{a}$ to $\frac{\pi}{a}$. Under the condition $|t_2| \ll |t_1|$, the band gap of the model is still at the Brillouin zone edge. A difference choice of the relative phases of the model parameters would be needed to have the gap at Γ (which is the case for PPI).

It is also possible to express the results of the model in terms of more physical parameters such as the energy gap and the HOMO and LUMO band widths:

$$W_c = \left[\Delta^2 + 4t_1^2\right]^{1/2} - \Delta + 4t_2, \tag{A11}$$

$$W_v = \left[\Delta^2 + 4t_1^2\right]^{1/2} - \Delta - 4t_2. \tag{A12}$$

Because in the realistic calculations the bands of interest may cross other bands far from the k corresponding to the gap, we consider partial ($\widetilde{W}_c$, $\widetilde{W}_v$) and not full band widths. These quantities are defined by the amplitude of the bands in a limited range of the Brillouin zone around the fundamental gap. This yields a much better agreement of the model bands with the calculated bands close to E_g, which is the energy range of interest. In order to extract the parameters E_g, t_1, and t_2 from our calculations, we used the following relations (under the restriction that the band gap is direct and located at the Brillouin zone edge $k = \pi/a$):

$$x_0 = x(k_0), \tag{A13}$$

$$t_2 = \frac{1}{4x_0}(\widetilde{W}_c - \widetilde{W}_v), \tag{A14}$$

$$t_1^2 = \frac{1}{2x_0}((\widetilde{W}_c - 2t_2\, x_0 + \Delta)^2 - \Delta^2). \tag{A15}$$

Following Ref. 8, once we have parametrized the model, we can give an analytical expression for the CBS (neglecting t_2^2 order terms):

$$\gamma(E) = \frac{(E - E_v)(E_c - E)}{2\left(t_1^2 + 2Et_2 - 2t_2\Sigma\right)} + 1, \tag{A16}$$

where Eq. (A1) connecting β to γ holds unchanged. The maximum of $\gamma(E)$ can be found analytically, and the resulting expression can be further simplified under the assumption $|t_2| \ll |t_1|$:

$$E_{\beta_{\max}} \sim \Sigma - t_2\left(\frac{\Delta}{t_1}\right)^2, \tag{A17}$$

$$\gamma(E_{\beta_{\max}}) \sim 1 + \frac{1}{8}\left(\frac{E_g}{t_1}\right)^2\left[1 + \frac{t_2^2}{t_1^2}\left(\frac{\Delta}{t_1}\right)^2\right]. \tag{A18}$$

APPENDIX B: COMPUTATIONAL DETAILS

The CRYSTAL09 software package[76] performs calculations based on the expansion of the crystalline orbitals as a linear

combination of a local basis set consisting of atom-centered Gaussian orbitals. A 6-31G* contraction double-valence (one s, two sp, and one d shells) quality basis set has been selected to describe carbon and nitrogen atoms; the most diffuse sp (d) exponents are $\alpha^{\mathrm{C}} = 0.1687$ (0.8) bohr^{-2} and $\alpha^{\mathrm{N}} = 0.2120$ (0.8) bohr^{-2}. The hydrogen atom basis set consists of a 31G* contraction (two s and one p shells): the most diffuse s and p exponents are 0.1613 and 1.1 bohr^{-2}. The self-consistent field procedure was converged to a tolerance in the total energy of $\Delta E = 2 \times 10^{-7}$ Ry per unit cell.[109] Reciprocal space sampling was performed on a Monkhorst-Pack grid with 12 **k** points. The thresholds for the maximum and r.m.s. forces (the maximum and the r.m.s. atomic displacements) have been set to 0.00090 and 0.00060 Ry/bohr (0.00180 and 0.00120 bohr).

The calculations performed with QE adopt a plane-wave basis set and norm-conserving pseudopotentials to describe the ion-electron interaction. The kinetic energy cutoff has been set to 45 Ry for wave functions. For ionic relaxation, total energy LDA and GGA calculations use a Monkhorst-Pack grid of 8, 6, and 6 **k** points for PE, PPV, and PPI, respectively (PA geometries are taken from the literature and not relaxed with QE). The convergence threshold on the atomic forces has been set to 10^{-3} Ry/bohr. A minimum distance of 20 bohr between chain replicas is used.

When performing *GW* calculations using SAX, the **k**-point grids have been made finer by using 50, 50, and 20 **k** points for PA, PE, and PPV, respectively. The long-range divergence of exchange-like Coulomb integrals is treated using a generalized version[110] of the approach given by Massidda *et al.*[111] The same approach has also been used when performing hybrid-DFT calculations with QE. Note that other schemes to treat exchange in one-dimensional systems have been proposed.[112–115] The Godby-Needs plasmon-pole model[67] has been used, setting the fitting energies at 0.0 and 2.0 Ry along the imaginary axis, for all cases. A kinetic energy cutoff of 6 Ry has been used to represent the polarizability P and the dynamic part of the screened Coulomb interaction W on a plane-wave basis, while a cutoff of 45 Ry has been used for the exchange operator. In order to converge the sums over empty states for the polarizability (self-energy), a total number of 288, 288, and 288 (288, 288, and 608) states has been used for PA, PE, and PPV, respectively. This corresponds to an equivalent transition-energy cutoff of 53, 53, and 35 eV (53, 53, and 44 eV). The interchain distance has been increased to $\simeq$30 bohr to control spurious interactions of periodic replica. The QP corrections are computed by evaluating the diagonal matrix elements of the self-energy operator $\langle n\mathbf{k}|\Sigma_{\mathrm{xc}}|n\mathbf{k}\rangle$, unless explicitly stated.

*Correspondence author: andrea.ferretti@unimore.it

[1] A. Nitzan and M. A. Ratner, Science **300**, 1384 (2003).
[2] A. Flood, J. Stoddart, D. Steuerman, and J. Heath, Science **306**, 2055 (2004).
[3] N. Agraït, A. L. Yeyati, and J. M. van Ruitenbeek, Phys. Rep. **377**, 81 (2003).
[4] J. P. Bourgoin, Lect. Notes Phys. **579**, 105 (2001).
[5] R. Holmlin, R. Haag, M. Chabinyc, R. Ismagilov, A. Cohen, A. Terfort, M. Rampi, and G. Whitesides, J. Am. Chem. Soc. **123**, 5075 (2001).
[6] M. L. Chabinyc, X. Chen, R. E. Holmlin, H. Jacobs, H. Skulason, C. D. Frisbie, V. Mujica, M. A. Ratner, M. A. Rampi, and G. M. Whitesides, J. Am. Chem. Soc. **124**, 11730 (2002).
[7] S. H. Choi, B. Kim, and C. D. Frisbie, Science **320**, 1482 (2008).
[8] J. K. Tomfohr and O. F. Sankey, Phys. Rev. B **65**, 245105 (2002).
[9] G. Peng, M. Strange, K. S. Thygesen, and M. Mavrikakis, J. Phys. Chem. C **113**, 20967 (2009).
[10] E. Prodan and R. Car, Phys. Rev. B **80**, 035124 (2009).
[11] H. Oevering, M. Paddonrow, M. Heppener, A. Oliver, E. Cotsaris, J. Verhoeven, and N. Hush, J. Am. Chem. Soc. **109**, 3258 (1987).
[12] H. Finklea and D. Hanshew, J. Am. Chem. Soc. **114**, 3173 (1992).
[13] J. Smalley, S. Feldberg, C. Chidsey, M. Linford, M. Newton, and Y. Liu, J. Phys. Chem. **99**, 13141 (1995).
[14] B. Paulson, K. Pramod, P. Eaton, G. Closs, and J. Miller, J. Phys. Chem. **97**, 13042 (1993).
[15] W. Davis, W. Svec, M. Ratner, and M. Wasielewski, Nature (London) **396**, 60 (1998).
[16] F. Lewis, T. Wu, X. Liu, R. Letsinger, S. Greenfield, S. Miller, and M. Wasielewski, J. Am. Chem. Soc. **122**, 2889 (2000).
[17] K. Fukui and K. Tanaka, Angew. Chem. Int. Ed. **37**, 158 (1998).
[18] S. O. Kelley and J. K. Barton, Science **283**, 375 (1999).
[19] F. Picaud, A. Smogunov, A. D. Corso, and E. Tosatti, J. Phys. Condens Matter **15**, 3731 (2003).
[20] A. L. Fetter and J. D. Walecka, *Quantum Theory of Many-Particle Systems* (McGraw-Hill, New York, 1971).
[21] L. Hedin, Phys. Rev. **139**, A796 (1965).
[22] L. Hedin and S. Lundqvist, Solid State Phys. **23**, 1 (1969).
[23] S. Y. Quek, H. J. Choi, S. G. Louie, and J. B. Neaton, Nano Lett. **9**, 3949 (2009).
[24] S. Kümmel and L. Kronik, Rev. Mod. Phys. **80**, 3 (2008).
[25] J. H. Burroughes, D. D. C. Bradley, A. R. Brown, R. N. Marks, K. Mackay, R. H. Friend, P. L. Burns, and A. B. Holmes, Nature (London) **347**, 539 (1990).
[26] S. H. Choi, C. Risko, M. C. R. Delgado, B. Kim, J.-L. Bredas, and C. D. Frisbie, J. Am. Chem. Soc. **132**, 4358 (2010).
[27] J. Tersoff, Phys. Rev. Lett. **52**, 465 (1984).
[28] W. Kohn, Phys. Rev. **115**, 809 (1959).
[29] L. He and D. Vanderbilt, Phys. Rev. Lett. **86**, 5341 (2001).
[30] A. Ferretti, B. Bonferroni, A. Calzolari, and M. Buongiorno Nardelli, WANT code (2007), available at: http://www.wannier-transport.org
[31] A. Ferretti, A. Calzolari, B. Bonferroni, and R. Di Felice, J. Phys. Condens. Matter **19**, 036215 (2007).
[32] N. Sai, M. Zwolak, G. Vignale, and M. Di Ventra, Phys. Rev. Lett. **94**, 186810 (2005).
[33] P. Bokes, J. Jung, and R. W. Godby, Phys. Rev. B **76**, 125433 (2007).
[34] S. Kurth, G. Stefanucci, C. O. Almbladh, A. Rubio, and E. K. U. Gross, Phys. Rev. B **72**, 035308 (2005).
[35] K. S. Thygesen and A. Rubio, Phys. Rev. B **77**, 115333 (2008).
[36] G. Vignale and M. Di Ventra, Phys. Rev. B **79**, 014201 (2009).
[37] H. Ness, L. K. Dash, and R. W. Godby, Phys. Rev. B **82**, 085426 (2010); H. Nesh and L. K. Dash, J. Phys. A-Math. Theor. **45**, 195301 (2012).
[38] S. Kurth, G. Stefanucci, E. Khosravi, C. Verdozzi, and E. K. U. Gross, Phys. Rev. Lett. **104**, 236801 (2010).

[39] A. Ferretti, A. Calzolari, R. Di Felice, F. Manghi, M. J. Caldas, M. Buongiorno Nardelli, and E. Molinari, Phys. Rev. Lett. **94**, 116802 (2005).

[40] A. Ferretti, A. Calzolari, R. Di Felice, and F. Manghi, Phys. Rev. B **72**, 125114 (2005).

[41] C. Toher, A. Filippetti, S. Sanvito, and K. Burke, Phys. Rev. Lett. **95**, 146402 (2005).

[42] S.-H. Ke, H. U. Baranger, and W. Yang, J. Chem. Phys. **126**, 201102 (2007).

[43] H. Mera, K. Kaasbjerg, Y. M. Niquet, and G. Stefanucci, Phys. Rev. B **81**, 035110 (2010).

[44] H. Mera and Y. M. Niquet, Phys. Rev. Lett. **105**, 216408 (2010).

[45] S. Lindsay and M. Ratner, Adv. Mater **19**, 23 (2007).

[46] M. D. Ventra, Adv. Mater. **21**, 1547 (2009).

[47] R. Landauer, Philos. Mag. **21**, 863 (1970).

[48] S. Datta and W. Tian, Phys. Rev. B **55**, 1914 (1997).

[49] T. Rangel, A. Ferretti, P. E. Trevisanutto, V. Olevano, and G. M. Rignanese, Phys. Rev. B **84**, 045426 (2011).

[50] M. Strange, C. Rostgaard, H. Hakkinen, and K. S. Thygesen, Phys. Rev. B **83**, 115108 (2011).

[51] P. Darancet, A. Ferretti, D. Mayou, and V. Olevano, Phys. Rev. B **75**, 075102 (2007).

[52] K. S. Thygesen and A. Rubio, J. Chem. Phys. **126**, 091101 (2007).

[53] A. Cehovin, H. Mera, J. H. Jensen, K. Stokbro, and T. B. Pedersen, Phys. Rev. B **77**, 195432 (2008).

[54] D. J. Mowbray, G. Jones, and K. S. Thygesen, J. Chem. Phys. **128**, 111103 (2008).

[55] S. Y. Quek, L. Venkataraman, H. J. Choi, S. G. Louie, M. S. Hybertsen, and J. B. Neaton, Nano Lett. **7**, 3477 (2007).

[56] P. Stephens, F. Devlin, C. Chabalowski, and M. Frisch, J. Phys. Chem. **98**, 11623 (1994).

[57] J. Perdew, M. Ernzerhof, and K. Burke, J. Chem. Phys. **105**, 9982 (1996).

[58] J. Muscat, A. Wander, and N. Harrison, Chem. Phys. Lett. **342**, 397 (2001).

[59] X. Blase, C. Attaccalite, and V. Olevano, Phys. Rev. B **83**, 115103 (2011).

[60] M. Jain, J. R. Chelikowsky, and S. G. Louie, Phys. Rev. Lett. **107**, 216806 (2011).

[61] S. Refaely-Abramson, R. Baer, and L. Kronik, Phys. Rev. B **84**, 075144 (2011).

[62] C. Rostgaard, K. W. Jacobsen, and K. S. Thygesen, Phys. Rev. B **81**, 085103 (2010).

[63] G. Onida, L. Reining, and A. Rubio, Rev. Mod. Phys. **74**, 601 (2002).

[64] M. S. Hybertsen and S. G. Louie, Phys. Rev. B **34**, 5390 (1986).

[65] M. S. Hybertsen and S. G. Louie, Phys. Rev. B **34**, 2920 (1986).

[66] F. Aryasetiawan and O. Gunnarsson, Rep. Prog. Phys. **61**, 237 (1998).

[67] R. W. Godby and R. J. Needs, Phys. Rev. Lett. **62**, 1169 (1989).

[68] J. Heyd, G. Scuseria, and M. Ernzerhof, J. Chem. Phys. **118**, 8207 (2003).

[69] J. P. Perdew, A. Ruzsinszky, G. I. Csonka, O. A. Vydrov, G. E. Scuseria, V. N. Staroverov, and J. Tao, Phys. Rev. A **76**, 040501 (2007).

[70] M. A. L. Marques, J. Vidal, M. J. T. Oliveira, L. Reining, and S. Botti, Phys. Rev. B **83**, 035119 (2011).

[71] P. E. Blöchl, O. Jepsen, and O. K. Andersen, Phys. Rev. B **49**, 16223 (1994).

[72] J. R. Yates, X. Wang, D. Vanderbilt, and I. Souza, Phys. Rev. B **75**, 195121 (2007).

[73] N. Marzari and D. Vanderbilt, Phys. Rev. B **56**, 12847 (1997).

[74] I. Souza, N. Marzari, and D. Vanderbilt, Phys. Rev. B **65**, 035109 (2001).

[75] D. R. Hamann and D. Vanderbilt, Phys. Rev. B **79**, 045109 (2009).

[76] R. Dovesi, V. R. Saunders, C. Roetti, R. Orlando, C. M. Zicovich-Wilson, F. Pascale, B. Civalleri, K. Doll, N. M. Harrison, I. J. Bush, P. D'Arco, and M. Llunell, CRYSTAL09 *User's Manual* (University of Torino, Torino, Italy, 2009).

[77] The local nonorthogonal basis set of CRYSTAL is orthogonalized ($S' = Id$; $H' = S^{-1/2} H S^{-1/2}$) to improve the numerical accuracy of the complex band structure interpolation. Only in the numerically critical case of polyethylene (PE), the CRYSTAL basis is not orthogonalized and a real-space cutoff of the Hamiltonian is applied [$H(R) = 0$ for $R \geqslant 3$ unit cells]. For the same system, a real-space cutoff has been applied to $H(R)$ also when using Wannier functions as a basis (for $R \geqslant 4$ unit cells).

[78] L. Martin-Samos and G. Bussi, Comput. Phys. Commun. **180**, 1416 (2009).

[79] P. Giannozzi, S. Baroni, N. Bonini, M. Calandra, R. Car, C. Cavazzoni, D. Ceresoli, G. L. Chiarotti, M. Cococcioni, I. Dabo, A. D. Corso, S. de Gironcoli, S. Fabris, G. Fratesi, R. Gebauer, U. Gerstmann, C. Gougoussis, A. Kokalj, M. Lazzeri, L. Martin-Samos, N. Marzari, F. Mauri, R. Mazzarello, S. Paolini, A. Pasquarello, L. Paulatto, C. Sbraccia, S. Scandolo, G. Sclauzero, A. P. Seitsonen, A. Smogunov, P. Umari, and R. M. Wentzcovitch, J. Phys. Condens. Matter **21**, 395502 (2009).

[80] M. V. Faassen and P. de Boeij, J. Chem. Phys. **120**, 8353 (2004).

[81] B. Kirtman, J. Toto, K. Robins, and M. Hasan, J. Chem. Phys. **102**, 5350 (1995).

[82] L. Rodríguez-Monge and S. Larsson, J. Chem. Phys. **102**, 7106 (1995).

[83] M. Rohlfing, M. Tiago, and S. Louie, Synth. Met. **116**, 101 (2001).

[84] M. L. Tiago, M. Rohlfing, and S. G. Louie, Phys. Rev. B **70**, 193204 (2004).

[85] M. Rohlfing and S. G. Louie, Phys. Rev. Lett. **82**, 1959 (1999).

[86] C. S. Yannoni and T. C. Clarke, Phys. Rev. Lett. **51**, 1191 (1983).

[87] Q. Zhu, J. Fischer, R. Zuzok, and S. Roth, Solid State Commun. **83**, 179 (1992).

[88] P. Puschnig and C. Ambrosch-Draxl, Phys. Rev. Lett. **89**, 056405 (2002).

[89] E. Prodan and R. Car, Nano Lett. **8**, 1771 (2008).

[90] M. Strange and K. S. Thygesen, Beilstein J. Nanotechnol. **2**, 746 (2011).

[91] In the case of COHSEX, the screening W is computed at the LDA level (W_0) and it is not updated during self-consistency.

[92] D. Varsano, *First Principles Description of Response Functions in Low Dimensional Systems*, Ph.D. thesis (2006).

[93] I. Tamblyn, P. Darancet, S. Y. Quek, S. A. Bonev, and J. B. Neaton, Phys. Rev. B **84**, 201402 (2011).

[94] M. L. Tiago, P. R. C. Kent, R. Q. Hood, and F. A. Reboredo, J. Chem. Phys. **129**, 084311 (2008).

[95] K. Kaasbjerg and K. S. Thygesen, Phys. Rev. B **81**, 085102 (2010).

[96] C. Faber, C. Attaccalite, V. Olevano, E. Runge, and X. Blase, Phys. Rev. B **83**, 115123 (2011).

[97] R. Rinaldi, R. Cingolani, K. M. Jones, A. A. Baski, H. Morkoc, A. DiCarlo, J. Widany, F. Della Sala, and P. Lugli, Phys. Rev. B **63**, 075311 (2001).

[98]M. Kemerink, S. F. Alvarado, P. Muller, P. M. Koenraad, H. W. M. Salemink, J. H. Wolter, and R. A. J. Janssen, Phys. Rev. B **70**, 045202 (2004).
[99]J. Tersoff, Phys. Rev. B **30**, 4874 (1984).
[100]L. Venkataraman, J. Klare, I. Tam, C. Nuckolls, M. Hybertsen, and M. Steigerwald, Nano Lett. **6**, 458 (2006).
[101]Y. S. Park, J. R. Widawsky, M. Kamenetska, M. L. Steigerwald, M. S. Hybertsen, C. Nuckolls, and L. Venkataraman, J. Am. Chem. Soc. **131**, 10820 (2009).
[102]M. Hybertsen, L. Venkataraman, J. Klare, A. Whalley, M. Steigerwald, and C. Nuckolls, J. Phys. Condens. Matter **20**, 374115 (2008).
[103]D. Wold, R. Haag, M. Rampi, and C. Frisbie, J. Phys. Chem. B **106**, 2813 (2002).
[104]B. Xu and N. Tao, Science **301**, 1221 (2003).
[105]C. C. Kaun, B. Larade, and H. Guo, Phys. Rev. B **67**, 121411 (2003).
[106]L. Venkataraman, J. E. Klare, C. Nuckolls, M. S. Hybertsen, and M. L. Steigerwald, Nature **442**, 904 (2006).
[107]J. He, F. Chen, J. Li, O. Sankey, Y. Terazono, C. Herrero, D. Gust, T. Moore, A. Moore, and S. Lindsay, J. Am. Chem. Soc. **127**, 1384 (2005).
[108]J. S. Meisner, M. Kamenetska, M. Krikorian, M. L. Steigerwald, L. Venkataraman, and C. Nuckolls, Nano Lett **11**, 1575 (2011).
[109]The Coulomb and exchange series are summed directly and truncated using overlap criteria with thresholds of 10^{-10}, 10^{-10}, 10^{-10}, 10^{-10}, and 10^{-20} as described previously;[116] the choice of these very severe thresholds has been dictated by the high accuracy required by the complex band structure calculations.
[110]To this aim, electrostatic interactions were cut off in real space for distances larger than the Wigner-Seitz supercell corresponding to the adopted **k**-point mesh (L. Martin-Samos, A. Ferretti, and G. Bussi, in preparation).
[111]S. Massidda, M. Posternak, and A. Baldereschi, Phys. Rev. B **48**, 5058 (1993).
[112]A. Marini, C. Hogan, M. Grüning, and D. Varsano, Comput. Phys. Commun. **180**, 1392 (2009).
[113]S. Ismail-Beigi, Phys. Rev. B **73**, 233103 (2006).
[114]Y. Li and I. Dabo, Phys. Rev. B **84**, 155127 (2011).
[115]C. A. Rozzi, D. Varsano, A. Marini, E. K. U. Gross, and A. Rubio, Phys. Rev. B **73**, 205119 (2006).
[116]C. Pisani, R. Dovesi, and C. Roetti, *Hartree-Fock Ab Initio Treatment of Crystalline Systems*, Vol. 48 of Lecture Notes in Chemistry (Springer-Verlag, Heidelberg, 1988).